Aalborg Universitet

AALBORG UNIVERSITY

Virtual Large-Scale Array Beamforming Analysis Using Measured Subarray Antenna Patterns

Zhang, Fengchun; Fan, Wei; Zhang, Jianhua; Pedersen, Gert F.

Link to publication from Aalborg University

Virtual Large-Scale Array Beamforming Analysis Using Measured Subarray Antenna Patterns

Fengchun Zhang, Wei Fan, Jianhua Zhang and Gert F. Pedersen

Abstract—An accurate and reliable massive MIMO channel model is crucial for supporting design and performance evaluation of such systems in the future. However, massive MIMO channel sounding systems are cost-prohibitive and complicated, where a large number of antenna elements and associated radio frequency (RF) transceiver chains are needed. Virtual large-scale arrays have been extensively utilized as an alternative for massive MIMO channel characterization. In this paper, we investigate virtual large-scale array systems formed by repositioning a real subarray systems for channel characterization. With this scheme, we have the flexibility to scale between system cost and system channel sounding capability. Based on this scheme, general beampatterns of subarrays and subarray-based virtual large-scale arrays are derived, based on measured complex antenna patterns of antenna elements on the subarray. Three real subarray antenna systems, i.e., a 16 element uniform rectangular array (URA) at 3.5 GHz, an 8 element uniform circular array (UCA) at 3.5 GHz, and an 8 element uniform linear array (ULA) at 10 GHz, were utilized to form the respective large-scale virtual arrays, i.e., a 128 element URA, a 48 element uniform cylinder array(UCyA) and a 64 element ULA, respectively. Beamforming analysis based on the measured complex radiation patterns of the real arrays are provided to demonstrate that virtual large-scale arrays can significantly improve the capability of multipath parameter detection compared with the subarrays. Therefore, such cost-effective systems are promising for characterization massive MIMO propagation channels.

Index Terms—Massive MIMO, channel characterization, subarray, virtual large-scale arrays.

I. INTRODUCTION

Due to the popularization of wireless devices, mobile traffic data has grown significantly in past years. Further, there is a growing demand for ubiquitous, reliable and high-speed wireless connectivity [1]. To deal with the surging data traffic growth and emerging applications, massive multiple-input multiple-output (MIMO) has arisen as a promising technology. It is further seen as an enabling technology for the coming fifth generation (5G) cellular systems [2]. Massive MIMO is a multi-user MIMO technology, where radio base stations (BSs) are equipped with a very large number of antennas to simultaneously serve many terminals in the same time-frequency resource [3]. Massive MIMO systems has gained significant interest, due to its capability of reducing system latency, improving signal power level, suppressing interference, and improving system capacity [4]. Accurate channel characterization of the massive MIMO systems is vital

Fengchun Zhang, Wei Fan and Gert F. Pedersen are with the APNET section at the Department of Electronic Systems, Faculty of Engineering and Science, Aalborg University, Denmark (email: {wfa}@es.aau.dk

Jianhua Zhang is with Beijing University of Posts and Telecommunications, China

for system design and performance evaluation of future 5G systems. Due to this, extensive efforts have been ongoing to record real world propagation channels for massive MIMO systems [5]–[9].

One straightforward massive MIMO channel measurement system is to utilize real large-scale arrays at the Tx and/or Rx side to record the channel characteristics. Several channel measurements based on large-scale antenna arrays were reported in the literature. A cylindrical array at 2.6 GHz, equipped with 64 dual-polarized patch antennas, was reported in [10]. Arrays of various types composed of 64 monopoles were utilized for channel sounding purposes in [11]. These systems are often capable of capturing time-variant channel characteristics. However, real large-scale antenna arrays require extensive efforts and long time in design, development and validation. Further, with many antennas, many radio frequency (RF) transceivers are required to record channels simultaneously in parallel structures, possibly combined with fast RF switches. Collecting a large quantity of data to accommodate long duration during sounding measurements at high sampling rates and across many channels is problematic. As a result, these systems are often cost-prohibitive and complicated.

Another much more widely utilized massive MIMO channel measurement system is so-called virtual array systems, where one antenna element is mechanically repositioned at predefined locations to form a 2D or 3D virtual antenna array [7], [12]–[19]. Only one antenna and one associated radio frequency (RF) transceiver chain are needed at the transmitter (Tx) and receiver (Rx) side, respectively. This system has been utilized both for indoor and outdoor channel sounding measurements. The measurement system is attractive and widely adopted, due to its simplicity, low cost and flexibility. However, it can only be applied in static environments, since it is assumed that channel profiles remain static for all element locations (i.e. antenna elements in the virtual array). Therefore, it requires that the total channel sounding time should be shorter than the channel coherence time, which is often violated in real world environments, especially when the number of measurement locations becomes large for massive MIMO systems.

A virtual large array (VLA) can be formed, via consecutively repositioning the real subarray at various predefined locations. This subarray-based VLA is scalable, since the number of the locations and the locations for the subarray can be arbitrarily set. With this scheme, we have the flexibility to scale between system cost and capability. The framework offers lower cost and more flexible array structure compared to real large-scale array systems. The cost of the formed

virtual large-scale array system is mainly determined by its real subarray, while the measurement time depends on number of locations of the subarray in the VLA. Another advantage of this framework is that existing channel sounding systems based on subarrays can be directly used for massive MIMO channel sounding purposes, without any additional cost. Noted that for VLA based channel sounding system, a real array is utilized for each position. It is therefore required as well that the channel profile should be remained static for different array element positions. Consider a virtual array of K elements, the measuring time is $T \times K$ with the single-antenna arrays presented in reference [7], [12]–[19], where T is the time to record the channel profile at one position. It is noted that the channel sounding time T to record channel profile per position is determined by the subarray channel sounder. With a subarray based VLA system, the measuring time is reduced to $T \times K/N$ in principle, where N is the element number in the real array (i.e. subarray). In this paper, we investigate the beamforming capabilities of VLA systems for channel sounding purpose.

VLAs based on single antenna system have been widely utilized for channel sounding measurements in the literature [7], [12]–[19]. However, few results have been published for VLAs based on real subarrays. In [8], [20], [21], a 256-element virtual large rectangular array formed by a 16 element uniform rectangular subarray was reported. The VLA was employed in an urban macro (UMa) scenario for channel sounding measurements. An outdoor measurement campaign with a scalable virtual cylinder array formed by a 7 element uniform linear array (ULA) was reported in [9]. However, beamforming capabilities of the formed VLA have not been addressed in the refereed papers, to the best knowledge of the authors.

In this paper, three real antenna arrays, i.e., a ULA, a uniform rectangular array (URA) and a uniform circular array (UCA), are utilized as the subarrays. The virtual large-scale ULA, URA and uniform cylinder array (UCyA) are formed via consecutively repositioning the subarrays at predefined positions, as illustrated in Fig. 1. Based on the measured complex radiation patterns of the antenna elements on the subarrays, beampatterns of the subarrays and the VLAs are derived in a general form for channel sounding purposes. Further, a numerical simulation results are provided to demonstrate the performance improvement of the VLAs for channel sounding.

II. SUBARRAYS

In this paper, three real antenna arrays are utilized as the subarrays to form the VLAs, as detailed in Table I. The coordinate system used in the paper is shown in Fig. 2. The elevation angle $\vartheta \in [-90^o, 90^o]$ is measured from the xy plane with $\vartheta > 0$ at the positive z-axis direction and the azimuth angle $\varphi \in [-180^o, 180^o]$ is measured from the x-axis on the xy plane with $\varphi > 0^o$ measured counter-clockwise.

In this section, we analyze the complex radiation patterns of the antenna elements measured with all antennas on the subarrays, where the complex radiation pattern for θ and ϕ
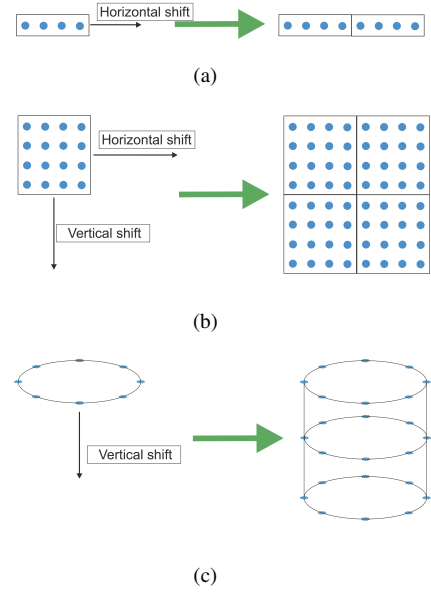

Fig. 1. An illustration of VLA ULA (a), VLA URA (b) and VLA UCyA (c) formed by the respective subarray ULA (a), URA (b), and UCA (c)
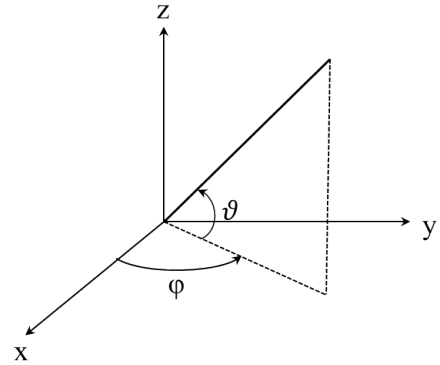

Fig. 2. Coordinate system.

polarization can be expressed as $g^\theta(\vartheta, \varphi) \cdot \exp[j\Omega^\theta(\vartheta, \varphi)]$ and $g^\phi(\vartheta, \varphi) \cdot \exp[j\Omega^\theta(\vartheta, \varphi)]$ with $g^\theta(\vartheta, \varphi)$ and $g^\phi(\vartheta, \varphi)$ representing the amplitude (gain) of θ polarized component and amplitude of ϕ polarized component, $\Omega^\theta(\vartheta, \varphi)$ and $\Omega^\phi(\vartheta, \varphi)$ phase pattern of θ polarized and ϕ polarized component, respectively. It is noted that the antenna field pattern is measured with a common phase reference point, so the spatial signature is included in the measured complex field pattern. The antenna pattern measurements were performed in large anechoic chambers. The subarrays were located in the quiet zone and a dual polarized probe antenna was rotated over a sphere to record the three dimensional complex radiation patterns for each antenna element.

III. BEAMFORMING ALGORITHM

Assume P plane waves impinge upon an array composed of N elements, the frequency response vector of the elements $\mathbf{h}(f) \in \mathbb{C}^{N \times Q}$ ($Q = 1$ for ULA and $Q = 2$ for both URA and

Table I
DESCRIPTION OF THE REAL SUBARRAYS

| Array configuration	ULA	URA	UCA
Number of elements	8	4×4	8
Element characteristics	Vertically polarized patch antenna; one port for each antenna.	Dual-polarized patch antenna; two ports for each antenna.	Dual-polarized patch antenna; two ports for each antenna.
Spacing in design	$d_y = 1$ cm (0.33λ)	$d_y = d_z = 4.1$ cm (0.48λ)	$d = 4.1$ cm (0.48λ with $r = 5.36$ cm)
Frequency	10 GHz	3.5 GHz	3.5 GHz
Photo	Fig. 3 (a)	Fig. 3 (b)	Fig. 3 (c)
Placement	on the y axis	on the yz plane	on the xy plane
Measured element patterns	2D patterns of 1° angle resolution. - Fig. 4(a) shows that the gain patterns of the elements are approximately symmetric around the x-axis and directive, with main beams around the boresight direction. - Fig. 4(b) compares the phase patterns of the elements ($*$ markers) and the slopes of ideal phase patterns based on array structure (dashed curves) at different scanning angles, both taking the 1st element as the phase center. The measured phase patterns are approximately linear. Note that the element spacing is set to $d_y = 0.84$ cm for the reference (i.e. dashed curves) as it gives the best matching. This might be caused by the positioning inaccuracy of the ULA in practical design.	3D patterns of 2° angle resolution (both ϑ and φ). - Fig. 5 depicts the radiation patterns of the 6-th element as an example, with (a) and (b) illustrating the θ and ϕ polarization, respectively. The pattern of port 1 and port 2 are complementary with $\pm 45^o$ crossing and the dominant power is distributed around the boresight direction, i.e. $(0^o, 0^o)$. The radiation patterns of the other elements are similar. - Fig. 6 plots the phase patterns of elements normalized with the phase of boresight, i.e. the phases of all elements calibrated to 0° at boresight direction. The example phase patterns at $(30^o, 60^o)$ are linear and have the similar slopes as the ideal phase curves across antenna elements.	3D patterns of 2° angle resolution (both ϑ and φ). - Fig. 7 shows the patterns on the azimuth plane (i.e. $\vartheta = 0^o$). All of the elements have similar patterns, with its main radiation beam of the n-th element towards $\psi_n = \frac{n-4}{N} \times 360^o, n \in [1,8]$ (i.e. the angular position of the n-th element). - Via circularly shifting ψ_n, 3D patterns of n-th element are similar to that of URA and hence they are omitted here. - Fig. 8 plots the phase patterns of the elements on the azimuth plane for θ polarization of port 1, where the phase pattern of the n-th element is shifted by ψ_n circularly. The phase patterns for $|\varphi - \psi_n| < 90^o$ match well with the ideal phase pattern (calculated based on the array structure). However, the phase errors are large for $|\varphi - \psi_n| \geq 90^o$, due to the weak gain patterns in these directions.
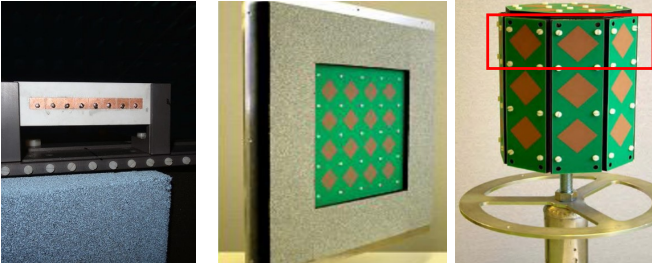
Fig. 3. An illustration of subarrays utilized: (a) ULA (b) URA and (c) UCA. Note that only eight antenna elements along the top ring of cylinder are used for the UCA (located inside the red box), as shown in Fig. 3 (c).

UCA denoting the antenna port for each element) as detailed in Tabel I, can be given as [22]

$$
\begin{aligned}
\mathbf{h}(f) &= \mathbf{e} \cdot \mathbf{A} \\
\mathbf{e} &= [\mathbf{e}^\theta, \mathbf{e}^\phi], \mathbf{e} \in \mathbb{C}^{1 \times 2P}, \mathbf{e}^\theta, \mathbf{e}^\phi \in \mathbb{C}^{1 \times P} \\
\mathbf{A} &= [\mathbf{A}^\theta; \mathbf{A}^\phi], \mathbf{A} \in \mathbb{C}^{2P \times N \times Q}, \mathbf{A}^\theta, \mathbf{A}^\phi \in \mathbb{C}^{P \times N \times Q},
\end{aligned}
\tag{1}
$$

where the superscripts θ and ϕ denote the θ and ϕ polarized components, respectively. The element of the path parameter vector $\mathbf{e}$ and the array manifold matrix $\mathbf{A}$ for θ or ϕ polariza-
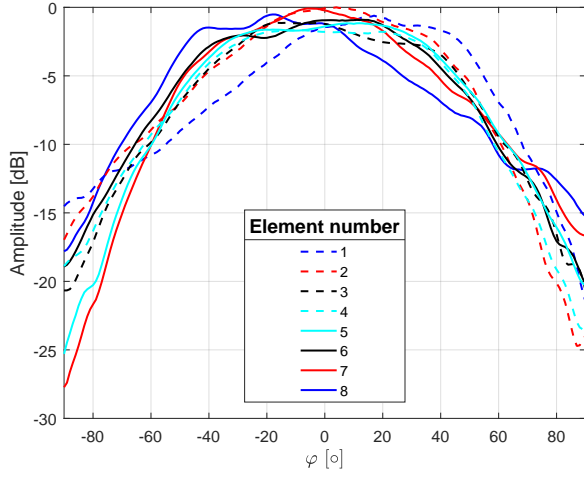
tion are expressed as

$$
\begin{aligned}
e_p^\eta &= \alpha_p^\eta \exp(-j2\pi f \tau_p) \\
a_{p,n,q}^\eta &= g_{n,q}^\eta(\vartheta_p, \varphi_p) \cdot \exp(j\mathbf{k}(f, \vartheta_p, \varphi_p) \cdot \mathbf{r}_n) \\
\eta &\in \{\theta, \phi\},
\end{aligned}
\tag{2}
$$

where τ_p, α_p^θ and α_p^ϕ represent the delay, the amplitude of the θ and ϕ polarization of the p-th path, respectively. $g_{n,q}^\theta(\vartheta, \varphi)$ and $g_{n,q}^\phi(\vartheta, \varphi)$ are gain patterns of the n-th element of port q at direction (ϑ, φ) for θ and ϕ polarization, respectively. Note that we have $g_{n,q}^\phi(\vartheta, \varphi) = 0$ for ULA as described in Table I, since the ULA is composed of vertically polarized patch antennas only. $\mathbf{k}(f, \vartheta, \varphi)$ is the wave vector and $\mathbf{r}_n$ is the location vector of the n-th element, which are written as
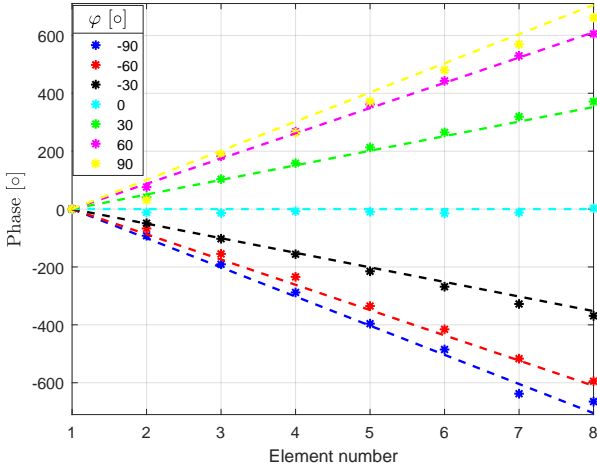
$$
\begin{aligned}
\mathbf{k}(f, \vartheta, \varphi) &= \frac{2\pi f}{c}[\cos\vartheta\cos\varphi, \cos\vartheta\sin\varphi, \sin\vartheta] \\
\mathbf{r}_n &= [x_n, y_n, z_n]^T,
\end{aligned}
\tag{3}
$$

With the beamforming algorithm, the beampattern of the arrays can be efficiently obtained via sweeping the weighting vector

$$
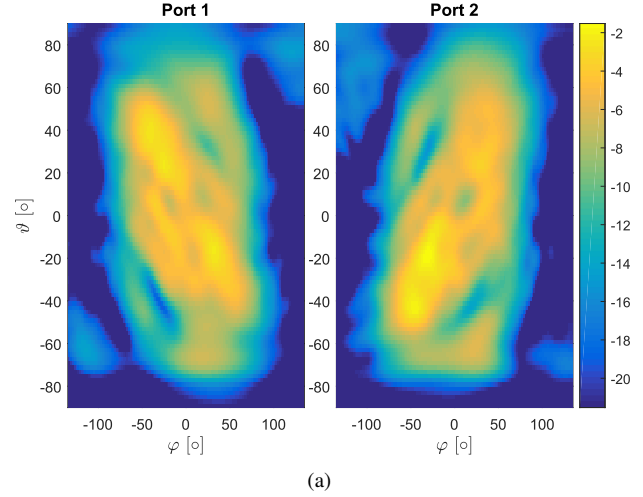\mathbf{b}(f, \vartheta, \varphi) = \mathbf{w}(f, \vartheta, \varphi) \cdot \mathbf{h}(f),
\tag{4}
$$

Fig. 4. Measured radiation patterns of ULA elements, (a) amplitude and (b) phase.

Fig. 5. Measured amplitude radiation patterns of the 6-th element of URA, (a) θ polarization and (b) ϕ polarization.

where $\mathbf{w}(f,\vartheta,\varphi) \in \mathbb{C}^{1 \times N}$ is the complex weight vector for the N elements and can be expressed as
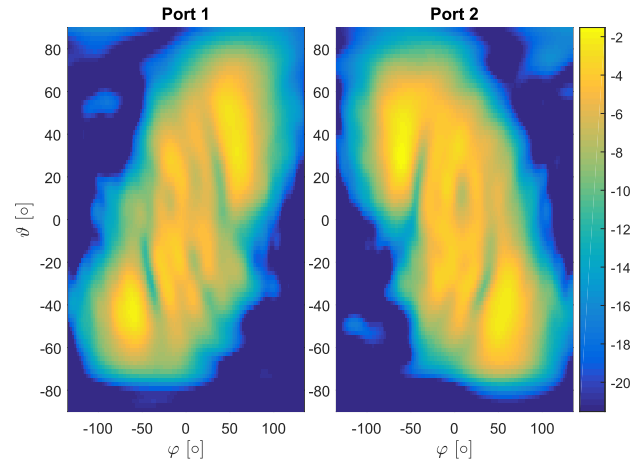
$$\mathbf{w}(f,\vartheta,\varphi) = [\hat{g}_1 \cdot \exp(-j\mathbf{k}(f,\vartheta,\varphi) \cdot \mathbf{r}_1), ..., \\ \hat{g}_N \cdot \exp(-j\mathbf{k}(f,\vartheta,\varphi) \cdot \mathbf{r}_N)], \quad (5)$$

where $\hat{g}_n$ and $[-\mathbf{k}(f,\vartheta,\varphi) \cdot \mathbf{r}_n]$ represent the amplitude tapering coefficient and phase of the complex weight for the n-th element, respectively. It is shown in Appendix A that the beampattern of port q can be written as

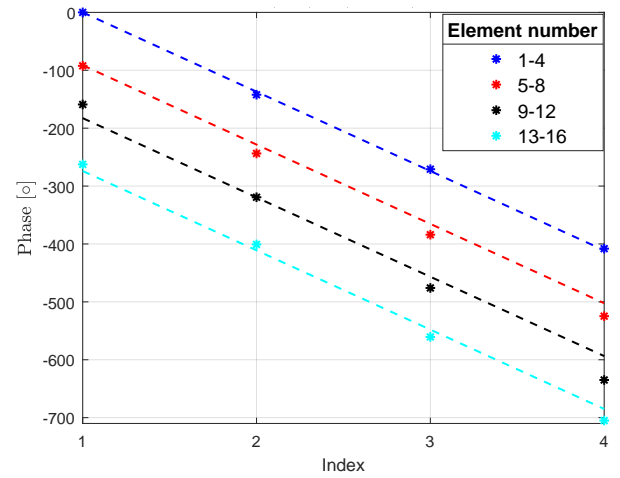$$b_q(f,\vartheta,\varphi) = v_{p,q}(f,\vartheta,\varphi) + i_q(f,\vartheta,\varphi), \quad (6)$$

Fig. 6. Measured phase patterns of URA elements for θ polarization of port 1 for $(\vartheta,\varphi) = (30^o, 60^o)$ with phase calibration.
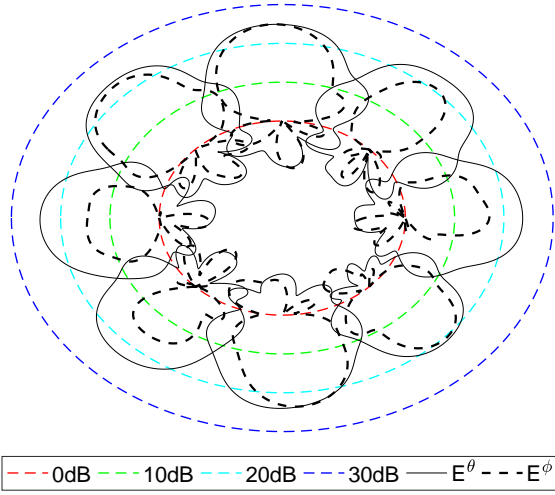
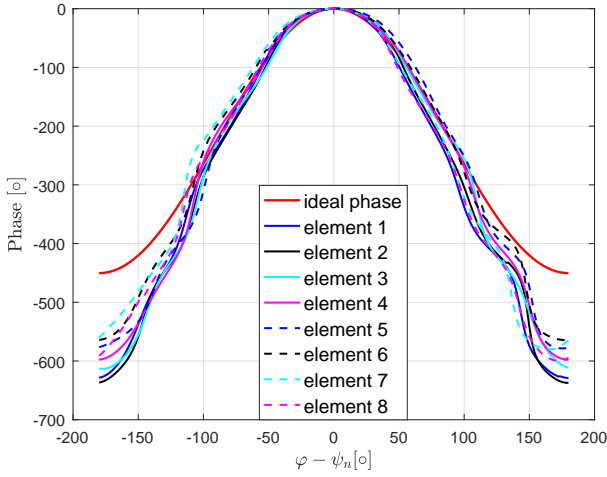Fig. 7. Measured element radiation patterns of the subarray UCA on azimuth plane.

Fig. 8. Measured phase patterns of the subarray UCA on the azimuth plane for θ polarization of port 1.

in which

$$i_q(f,\vartheta,\varphi) = \sum_{i=1,i\neq p}^{P} v_{i,q}(f,\vartheta,\varphi)$$

$$v_{p,q}(f,\vartheta,\varphi) = |v_{p,q}(f,\vartheta,\varphi)| \exp(-j2\pi f\tau_p)$$

$$|v_{p,q}(f,\vartheta,\varphi)| = |\sum_{n=1}^{N} \hat{g}_n[\alpha_p^\theta g_{n,q}^\theta(\vartheta_p,\varphi_p) + \alpha_p^\phi g_{n,q}^\phi(\vartheta_p,\varphi_p)]$$
$$\cdot \exp\{j[\mathbf{k}(f,\vartheta_p,\varphi_p) - \mathbf{k}(f,\vartheta,\varphi)] \cdot \mathbf{r}_n\}|.$$
(7)

To estimate the path parameters $\{\alpha_p^\theta, \alpha_p^\phi, \tau_p, \vartheta_p, \varphi_p\}$, we need to guarantee that:

- at the target angle (ϑ_p, φ_p), we have a peak (main beam) exist with the peak value of $|v_{p,q}(f,\vartheta,\varphi)|$ and the interference from other paths, i.e. $|i_q(f,\vartheta,\varphi)|$ approaches 0;
- for $\vartheta \neq \vartheta_p$ or $\varphi \neq \varphi_p$, the sidelobes represented by $|b_q(f,\vartheta,\varphi)|$ approach 0.

Note that $v_{p,q}(f,\vartheta,\varphi)$ in (7) can meet the above requirements due to the orthogonality of complex exponentials [23]. Therefore, the incident direction (ϑ_p, φ_p) can be determined for $p \in [1, P]$. The path delay parameter τ_p can be obtained via performing inverse Fourier transform of $b_q(f,\vartheta,\varphi)$. For (ϑ_p, φ_p), neglecting the interfering pattern from other paths, the beampattern of the array in (6) becomes

$$|b_q(f,\vartheta_p,\varphi_p)| = |v_{p,q}(f,\vartheta_p,\varphi_p)|$$
$$= \alpha_p^\theta \cdot G_q^\theta(\vartheta_p,\varphi_p) + \alpha_p^\phi \cdot G_q^\phi(\vartheta_p,\varphi_p),$$
(8)

where $G_q^\theta(\vartheta_p,\varphi_p)$ and $G_q^\phi(\vartheta_p,\varphi_p)$ can be given according to equation (7)

$$G_q^\eta(\vartheta_p,\varphi_p) = \sum_{n=1}^{N} \hat{g}_n g_{n,q}^\eta(\vartheta_p,\varphi_p)$$
(9)
$$\eta \in \{\theta, \phi\}.$$

For ULA, the amplitude of the p-th path can be obtained directly from (8),

$$\alpha_p^\theta = \frac{|b_1(f,\vartheta_p,\varphi_p)|}{G_1^\theta(\vartheta_p,\varphi_p)}.$$
(10)

While the corresponding amplitudes $(\alpha_p^\theta, \alpha_p^\phi)$ of URA and UCA are obtained from (8) as:

$$\begin{bmatrix} \alpha_p^\theta \\ \alpha_p^\phi \end{bmatrix} = \begin{bmatrix} G_1^\theta(\vartheta_p,\varphi_p) & G_1^\phi(\vartheta_p,\varphi_p) \\ G_2^\theta(\vartheta_p,\varphi_p) & G_2^\phi(\vartheta_p,\varphi_p) \end{bmatrix}^{-1} \begin{bmatrix} |b_1(f,\vartheta_p,\varphi_p)| \\ |b_2(f,\vartheta_p,\varphi_p)| \end{bmatrix},$$
(11)

where $(\cdot)^{-1}$ and $(\cdot)^T$ denote the inverse and transpose operators, respectively.

As a summary, parameters $\{\alpha_p^\theta, \alpha_p^\phi, \tau_p, \vartheta_p, \varphi_p\}$ for $p \in [1, P]$ can be determined based on the array system by applying beamforming algorithms. Compared to high resolution algorithms, e.g. space alternating generalized expectation-maximization (SAGE) or maximum likelihood estimation (MLE), the beamforming algorithms is more robust and computationally faster. For high resolution algorithms, different parameter domains (e.g. amplitude, delay, angle) for each path should be estimated seperately, which often suffers from high computation complexity. With the beamforming algorithm, the beamforming power pattern can be efficiently obtained via sweeping the weighting vector. Quantitative complexity analysis of various algorithms can be found in the exiting literature, e.g. [15], [22], [24], and therefore is left out in this paper.

A. Subarray beamforming

The discussions above apply to both single-antenna based virtual arrays and real arrays. For the single-antenna based virtual arrays, the gain patterns of all antenna elements are identical, i.e., for the ULA and URA, we have $g_{n,q}^\eta(\vartheta_p,\varphi_p) = g_q^\eta(\vartheta_p,\varphi_p)$. For the UCA, we have $g_{n,q}^\eta(\vartheta_p,\varphi_p) = g_q^\eta(\vartheta_p,\varphi_p - \psi_n), n \in [1, N], \eta \in \{\theta, \phi\}$, where $\psi_n = (n-4)/N \times 360^o$ is the angular position of the n-th element. Phase patterns for all antenna elements can be calculated from the array structure. Once the gain pattern of an element and the positions of the

elements are precisely known, we can calculate the complex weight vector $\mathbf{w}(f,\vartheta,\varphi)$ as in (5).

For the real antenna arrays, the gain patterns of the elements, though similar, are different due to mutual coupling, edge effect and practical designs. The phase patterns are embedded in the measured radiation patterns. That is, the complex weight vector $\mathbf{w}(f,\vartheta,\varphi)$ can be formed by directly using the measured complex radiation patterns of the elements without the knowledge of the element positions, e.g. $\mathbf{w}(f,\vartheta,\varphi) = (\bar{\mathbf{a}}_q^\eta(f,\vartheta,\varphi))^H$, where $\bar{\mathbf{a}}_q^\eta(f,\vartheta,\varphi) \in \mathbb{C}^{N\times 1}$ is the measured complex radiation pattern vector of the array elements of port q with $\eta \in \{\theta, \phi\}$ and $(\cdot)^H$ denotes the Hermitian transpose operator.

Note that if the real antenna array is composed of directional antennas, phase patterns might be not accurate in directions where gain patterns are weak. Therefore, paths impinging with the direction within this region can not be accurately detected.

B. VLA beamforming

We now consider the properties of the VLAs realized by repositioning the subarrays M times (i.e. M identical subarrays), as illustrated in Fig. 1. Similar to the discussions about the subarrays, the corresponding frequency response vector of the elements for VLA can be expressed as

$$\underline{\mathbf{h}}(f) = \mathbf{e} \cdot \underline{\mathbf{A}}, \tag{12}$$

where the array manifold matrix $\underline{\mathbf{A}} \in \mathbb{C}^{2P\times NM\times Q}$ can be extended from $\mathbf{A}$ in (2) and (1) with its elements given by

$$\begin{aligned}\underline{a}_{p,\underline{n},q}^\eta &= a_{p,n,q}^\eta \cdot \exp(j\mathbf{k}(f,\vartheta_p,\varphi_p)\cdot\underline{\mathbf{r}}_m),\\\underline{n} &= n + m*N, n \in [1,N], m \in [0,M-1] \quad (13)\\\eta &\in \{\theta,\phi\}.\end{aligned}$$

where $\underline{\mathbf{r}}_m = [\underline{x}_m, \underline{y}_m, \underline{z}_m]^T$ is the location vector of the center of the m-th subarray and $a_{p,n,q}^\eta$ is defined in (2). According to the equations (4)-(7) and Appendix A, the similar derivation can be done to obtain the beampattern of VLA,

$$\underline{b}_q(f,\vartheta,\varphi) = \underline{v}_{p,q}(f,\vartheta,\varphi) + \underline{i}_q(f,\vartheta,\varphi), \tag{14}$$

where $\underline{i}_q(f,\vartheta,\varphi)$ is defined similar to $i_q(f,\vartheta,\varphi)$ in (7) as

$$\underline{i}_q(f,\vartheta,\varphi) = \sum_{i=1,i\neq p}^{P} \underline{v}_{i,q}(f,\vartheta,\varphi). \tag{15}$$

For the detailed derivation of the VLA beampattern term $\underline{v}_{p,q}(f,\vartheta,\varphi)$, please refer to Appendix B. The similar decomposed form as in [24] can be found as,

$$\underline{v}_{p,q}(f,\vartheta,\varphi) = v_{p,q}(f,\vartheta,\varphi) \cdot v_p^{iso}(f,\vartheta,\varphi), \tag{16}$$

where $v_{p,q}(f,\vartheta,\varphi)$ is beampattern term of the subarray defined in (7) and $v_p^{iso}(f,\vartheta,\varphi)$ denotes the beampattern of the antenna array composed of isotropic elements. $v_p^{iso}(f,\vartheta,\varphi)$ is given as

$$v_p^{iso}(f,\vartheta,\varphi) = \sum_{m=1}^{M} \exp\{j[\mathbf{k}(f,\vartheta_p,\varphi_p) - \mathbf{k}(f,\vartheta,\varphi)]\cdot\underline{\mathbf{r}}_m\}. \tag{17}$$

$v_p^{iso}(f,\vartheta,\varphi)$ can be further expressed by the product of beampattern term of the ULA (composed of isotropic elements) in

x-, y- and z-directions [23], [25], i.e. equation (C.1), which is shown in Appendix C.

Comparing with the beampattern of subarray $v_{p,q}(f,\vartheta,\varphi)$, narrower beamwidth and lower sidelobes can be achieved for the beampattern of VLA $\underline{v}_{p,q}(f,\vartheta,\varphi)$, due to the larger aperture of the virtual array. However, the gating lobes might occur for $v_p^{iso}(f,\vartheta,\varphi)$ (as shown in Fig. 6 in [24]), if the inter element spacing (i.e. subarray separation) is larger than $\lambda/2$, based on the (C.1)-(C.3). According to (16), the beampattern of VLA $\underline{v}_{p,q}(f,\vartheta,\varphi)$ is obtained by shaping the beampattern of subarray $v_{p,q}(f,\vartheta,\varphi)$ with $v_p^{iso}(f,\vartheta,\varphi)$. Therefore, the main beam is shaped to be narrower and the sidelobes are attenuated (except that the sidelobes remain unchanged at the directions that the peaks of the grating lobes exist). Note that the grating lobes will not appear if the inter-element spacing of VLA is smaller than $\lambda/2$.

To set the number of repostioning positions of subarrays, i.e., M, we need to consider the measuring time (to ensure the measured channel is relative static), the desired directivity of the VLA and the aperture of the VLA to satified the far-field assumption. In general, the number of repositioning positions M is not restricted by the element number of subarray N to form the VLA, while the locations of the subarrays need to be designed to avoid the grating lobes and the antenna element overlap of the adjacent subarrays.

IV. SIMULATION RESULTS

A. Subarray ULA and subarray-based VLA ULA
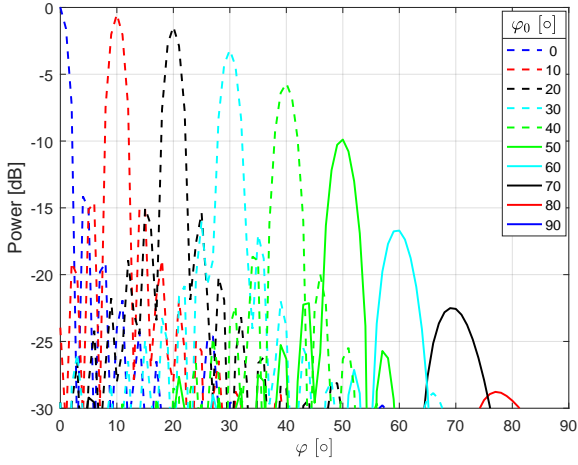
The beampatterns of the subarray ULA based on (7) with scanning azimuth angle $\varphi_0 \in [0^o, 90^o]$ are shown in Fig. 9(a). The beampatterns with scanning angle $\varphi_0 \in [-90^o, 0^o]$ are symmetric to those in $\varphi_0 \in [0^o, 90^o]$. The peak of the subarray beam generally follows the target scanning angle φ_0. However, the performance deteriorates as the φ_0 moves away from the boresight direction. For angles $\varphi_0 \in [50^o, 90^o]$, angles of the beam peaks differ from the target angles due to the inaccurate phase patterns in this angle region. Beams formed by the ULA suffer from wide beamwidth due to limited antenna element number and array aperture, as expected.

By shifting the subarray ULA along the y-axis $M = 8$ times with equal element spacing over the whole large-scale array, we can form a virtual large-scale ULA, as shown in Fig. 1(a). The formed large-scale ULA consists of 64 antenna elements. The beampatterns of the virtual ULA based on (14) with scanning azimuth angle $\varphi_0 \in [0^o, 90^o]$ can be obtained, as plotted in Fig. 9(b). Note that only the beampatterns for $\varphi \geqslant 0$ are plotted due to that the element radiation patterns are symmetric about x-axis (i.e. $\varphi = 0^o$) as shown in Fig. 4. Based on the results shown in Fig. 9, we can conclude that:

- The peak power decreases as $|\varphi_0|$ increases, which is consistent with the element radiation power distributed over φ;
- The peaks for angles $|\varphi_0| > 70^o$ are not reliable, due to the inaccurate phase information in these directions;
- Comparing with the beampatterns of the subarray ULA in Fig. 9(a), the peak positions of the virtual ULA are more accurate, with narrower main beamwidth and lower
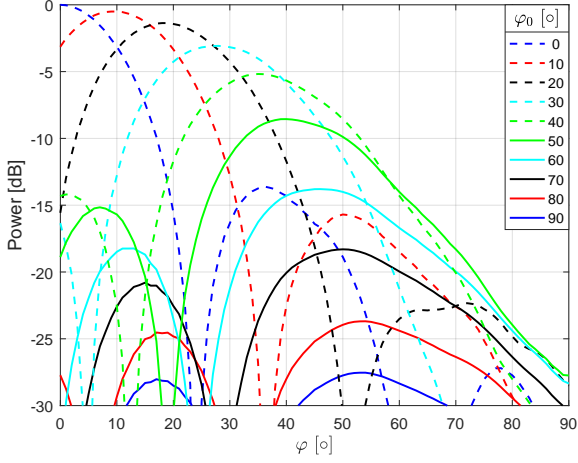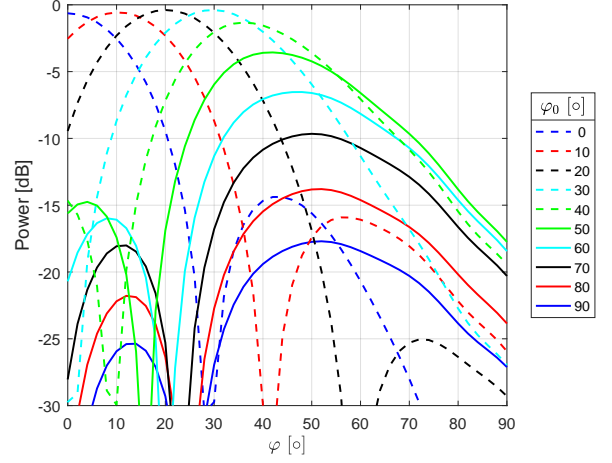
(a)

(b)

Fig. 9. Beampatterns of the subarray ULA (a) and the VLA (b) with $\varphi_0 \in [0^o, 90^o]$.

(a)

(b)

Fig. 10. Beampatterns of the subarray URA (a) and the virtual URA (b) with $\varphi_0 \in [0^o, 90^o]$ on the azimuth plane.

sidelobes. This is introduced by the increased aperture of the array.
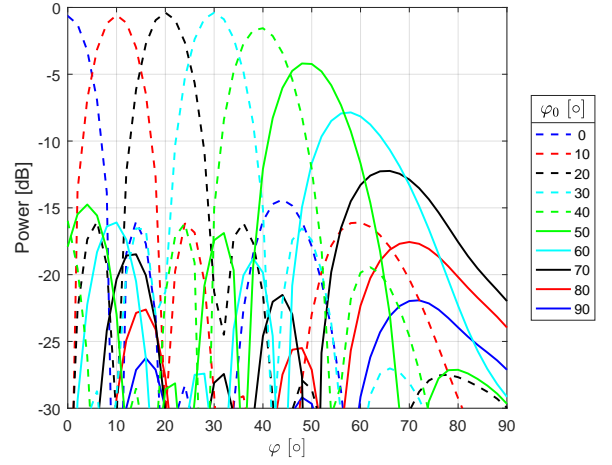
B. Subarray URA and subarray-based VLA URA

The beampatterns of the subarray array URA are similar on the azimuth plane (i.e. scanning azimuth angle φ with elevation angle fixed $\vartheta_0 = 0^o$) and on the elevation plane (i.e. scanning elevation angle ϑ with azimuth angle fixed $\varphi_0 = 0^o$). Therefore, we only demonstrate the beampatterns of the arrays on the azimuth plane for simplicity. The beampatterns of the subarray URA on azimuth plane with $\varphi_0 \in [0^o, 90^o]$ are shown in Fig. 10(a). Similar to the discussions for subarray ULA, the peak of the subarray beam generally follows the target azimuth angle $\varphi_0 \in [0^o, 40^o]$. For azimuth angles $\varphi_0 \in [50^o, 90^o]$, the beam peaks differ from the target scanning angles due to the inaccurate element phase patterns.

The virtual URA composed of $M = 4 \times 4$ subarray URAs is formed by repositioning the subarray URA along y-axis direction and z-axis direction with $\underline{d}_y = \underline{d}_z = 4d_y$, respectively, as illustrated in Fig. 1(b). The formed virtual large-scale URA consists of 256 equally spaced antenna elements.

The beampatterns of the virtual URA on azimuth plane with $\varphi_0 \in [0^o, 90^o]$ are shown in Fig. 10(b).

Similar to the ULA case, the peak power changes with φ_0, which agrees well with the element radiation power distribution over φ. The VLA URA can detect the path with incident angle $\varphi_0 \in [-70^o, 70^o]$. The virtual URA outperforms the subarray URA, since the peak positions of the virtual URA are more accurate and beampatterns have much narrower beam width and much lower side-lobes.

C. Subarray UCA and subarray-based VLA UCyA

The beampatterns of subarray UCA and the element radiation patterns on the azimuth plane are shown in Fig. 11. For the subarray beampatterns, the scanning angles are selected to be the element angular positions. We can see that the beam width of subarray UCA is much narrower than that of the element patterns, as expected. Note that the UCA can steer the beam to any direction on the azimuth plane, as illustrated in Fig. 11 (red curve), where the scanning angle is $\varphi = 30^o$.

A virtual UCyA can be realized by repositioning the subarray UCA along the z axis with $\underline{d}_z = 41$ mm (0.48λ at $f = 3.5$
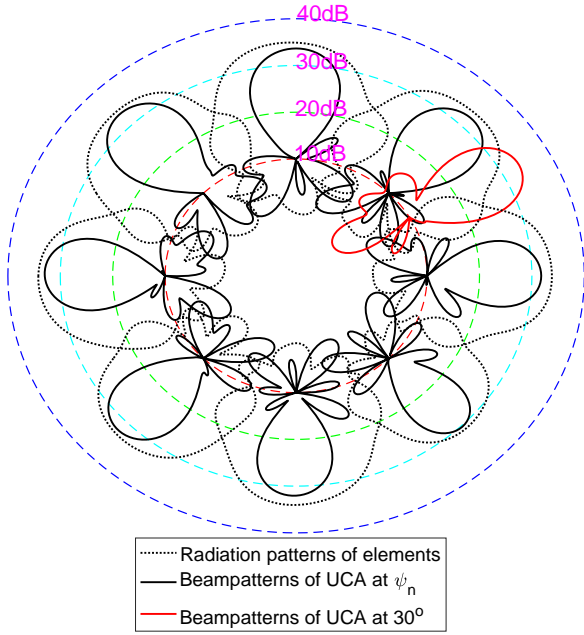
Fig. 11. Beampatterns of the subarray UCA comparing with the element radiation patterns on the azimuth plane.

GHz) with $M = 6$, as illustrated in Fig. 1(c). The formed virtual large-scale UCyA consists of 48 antenna elements. Comparing with the subarray UCA, the aperture of the virtual UCyA only increases in z axis direction. Therefore, the angle resolution in elevation domain will be improved, while the resolution in azimuth domain remains unchanged.

The beampatterns of the subarray UCA and the virtual UCyA with $\vartheta_0 \in [-90^o, 90^o]$ are shown in Fig. 12. We can see that the subarray UCA could not detect any ϑ_0 due to the limited aperture of the UCA and the directivity of UCA elements. The virtual UCyA can detect the ϑ_0 due to the increased aperture along z-axis. With the formed virtual UCyA, the path with incident angle $\vartheta_0 \in [-70^o, 70^o]$ can be detected.

D. Multipath detection

To demonstrate the multipath detection performance of the subarray and the subarray-based VLA, the subarray URA and the virtual URA are used. Three paths of single polarization with equal power impinging upon the subarray URA and the virtual URA are assumed for simplicity, where the incident directions $(\vartheta_p, \varphi_p), p \in [1, 3]$ are $(-30^o, -60^o)$, $(0^o, 0^o)$ and $(46^o, 30^0)$, respectively. It is noted that the subarray URA and UCA and their extensions to VLAs are capable of estimating dual polarized multipath components, as discussed in Section III. The power angle profiles for the subarray URA and the virtual URA are shown in Fig. 13. It is apparent that the parameters of the paths, i.e. incident angles and amplitudes, can be detected more accurately with the VLA URA, due to the much narrower beamwidth and lower sidelobes that it achieves. The beampattern achieved with subarray URA suffers from hig sidelobes and wide main beamwidth.
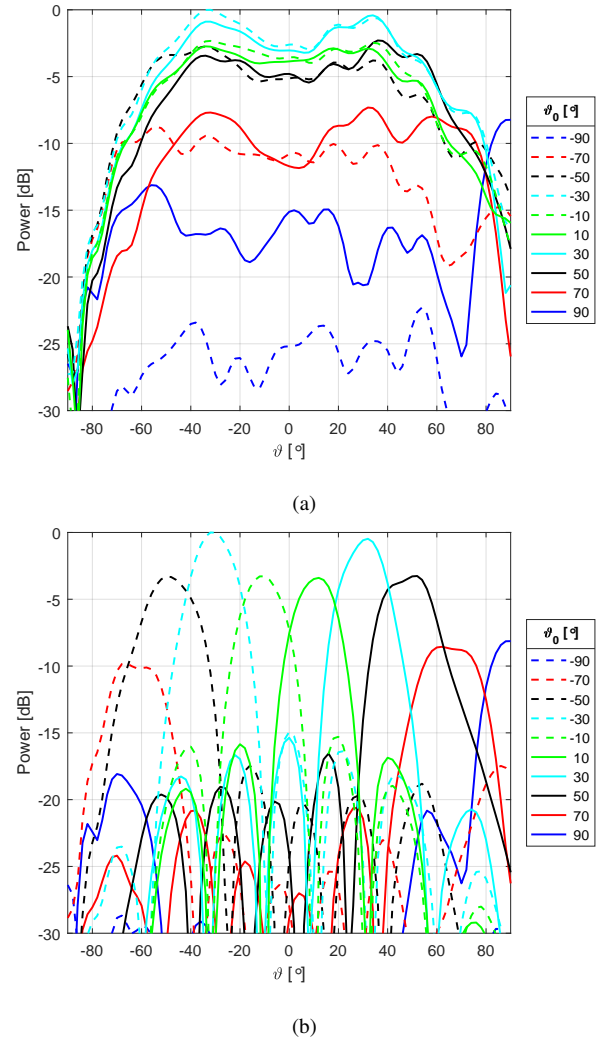

(a)

(b)

Fig. 12. Beampatterns of the subarray UCA (a) and the virtual UCyA (b) with $\vartheta_0 \in [-90^o, 90^o]$ by fixing $\varphi_0 = 0^o$.

V. CONCLUSION

In this paper, virtual large-scale arrays, formed by repositioning real subarray systems, are investigated for massive MIMO channel sounding purposes. Unlike results published in the literature where virtual array are constructed by repositioning single antenna systems, our work proposed a general framework to form virtual arrays, where virtual array element can be single antenna or real subarray antennas. This improvement can significantly reduce the measurement time (depending on real subarray element number), compared to virtual arrays based on single antenna system. With the virtual large scale array framework, massive MIMO channel sounding measurement can be performed without any additional cost of the system where only a small number of antennas are utilized. Further, we have the flexibility to scale between system cost and system channel sounding capability in time-variant propagation environments. Existing channel sounding systems which are equipped with real arrays of few antennas, can be readily utilized for massive MIMO channel sounding purposes, based on the proposed virtual array schemes.

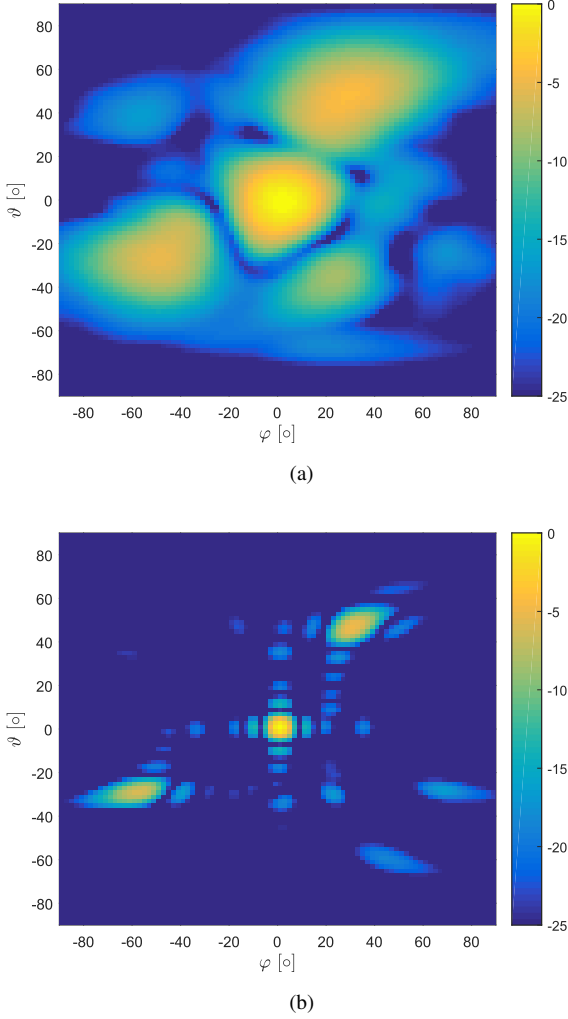The measured antenna element patterns demonstrated that

Fig. 13. Power angle profiles for the subarray URA (a) and the virtual URA (b).

the measured phased patterns agree well with the ideal phase patterns calculated from array structure in directions where antenna gain patterns are strong. However, phase errors (i.e. deviations between measured phase patterns and expected phase patterns based on array structure) exist in directions where the gain patterns are weak. As a result, the form beampatterns are accurate only in the directions where array element gain patterns are not weak (i.e. accurate phase patterns in the directions). The results were demonstrated for the subarray ULA, URA and UCA respectively.

Three real antenna arrays, i.e., a ULA, a URA and a UCA, are used as the subarrays to form the virtual large scale arrays, respectively. The general analytic beampatterns of subarrays and subarray-based VLA are derived, based on the measured radiation patterns of the subarray elements. The beamforming results show that the formed virtual large-scale array presents narrower main-lobe, lower side-lobes and more accurate beamforming capabilities compared to subarray systems. In practical measurements, the virtual array configuration, i.e. real subarray placement and number of subarrays, should be determined based on the channel coherence time and requirement on angle resolution in azimuth and elevation domains. There are some logical extensions of current work. For example, the proprosed beamformer algorithm for large virtual array should be applied to analyze recorded channel sounding data in real measurements.

APPENDIX A

Let

$$u_{i,n,q} = e_i^\theta \cdot a_{i,n,q}^\theta + e_i^\phi \cdot a_{i,n,q}^\phi$$
$$= [e_i^\theta g_{n,q}^\theta(\vartheta_i, \varphi_i) + e_i^\phi g_{n,q}^\phi(\vartheta_i, \varphi_i)] \cdot \exp[j\mathbf{k}(f, \vartheta_i, \varphi_i) \cdot \mathbf{r}_n],$$

(A.1)

where $i \in [1, P]$, $n \in [1, N]$ and q denote path index, element index and port index, respectively. The (n, q)-th element of $h(f)$ can be obtained by introducing (A.1) in (1) as

$$h_{n,q}(f) = \sum_{i=1}^{P} u_{i,n,q}$$
$$= u_{p,n,q} + \sum_{i=1, i \neq p}^{P} u_{i,n,q}.$$

(A.2)

Via substituting (A.2) into equation (4), The q-th element of $\mathbf{b}(f, \vartheta, \varphi)$ can be obtained as

$$b_q(f, \vartheta, \varphi) = \sum_{n=1}^{N} w_n(f, \vartheta, \varphi) \cdot h_{n,q}(f)$$
$$= \sum_{n=1}^{N} w_n(f, \vartheta, \varphi) \cdot (u_{p,n,q} + \sum_{i=1, i \neq p}^{P} u_{i,n,q})$$
$$= \{\sum_{n=1}^{N} w_n(f, \vartheta, \varphi) \cdot u_{p,n,q}\}$$
$$+ \{\sum_{n=1}^{N} w_n(f, \vartheta, \varphi) \cdot \sum_{i=1, i \neq p}^{P} u_{i,n,q}\}$$
$$= v_{p,q}(f, \vartheta, \varphi) + i_q(f, \vartheta, \varphi),$$

(A.3)

where the beampattern is decomposed into two terms, i.e., $v_{p,q}(f, \vartheta, \varphi)$ and $i_q(f, \vartheta, \varphi)$, substituting the two $\{\cdot\}$ terms, respectively.

Appendix B

Similar to the derivation in Appendix A, we define

$$\underline{u}_{p,\underline{n},q} = e_p^\theta \cdot \underline{a}_{p,\underline{n},q}^\theta + e_p^\phi \cdot \underline{a}_{p,\underline{n},q}^\phi \tag{B.1}$$

The equation (13) can connect the $\underline{u}_{p,\underline{n},q}$ with $u_{p,n,q}$ defined in (A.1) as

$$\begin{aligned}
\underline{u}_{p,\underline{n},q} &= [e_p^\theta \cdot a_{p,n,q}^\theta + e_p^\phi \cdot a_{p,n,q}^\phi] \cdot \Theta_m(\vartheta_p, \varphi_p) \\
&= u_{p,n,q} \cdot \Theta_m(\vartheta_p, \varphi_p), \\
\underline{n} &= n + m * N, n \in [1, N], m \in [0, M],
\end{aligned} \tag{B.2}$$

where $\Theta_{p,m}$ represents the extra phase introduced by the VLA for the p-th path at the m-th subarray, which is given by

$$\Theta_m(\vartheta_p, \varphi_p) = \exp[j\mathbf{k}(f, \vartheta_p, \varphi_p) \cdot \underline{\mathbf{r}}_m]. \tag{B.3}$$

The complex weight vector for VLA $\underline{\mathbf{w}}(f, \vartheta, \varphi) \in \mathbb{C}^{1 \times MN}$ can be chosen by extending $\mathbf{w}(f, \vartheta, \varphi)$. The $\underline{n}$-th element of the VLA weight vector could be selected as

$$\begin{aligned}
\underline{w}_{\underline{n}}(f, \vartheta, \varphi) &= \hat{g}_n \cdot \exp[-j\mathbf{k}(f, \vartheta, \varphi) \cdot (\mathbf{r}_n + \underline{\mathbf{r}}_m)] \\
&= w_n(f, \vartheta, \varphi) \cdot \Theta_m^*(\vartheta, \varphi),
\end{aligned} \tag{B.4}$$

where $w_n(f, \vartheta, \varphi)$ is the n-th element of the subarray defined in (5) and $(\cdot)^*$ denotes conjugate operator. Similar to the decomposing in (A.3), the beampattern term of VLA $\underline{v}_{i,q}(f, \vartheta, \varphi)$ can be obtained by substituting (B.2) and (B.4) into the following equation

$$\begin{aligned}
\underline{v}_{p,q}(f, \vartheta, \varphi) &= \sum_{\underline{n}}^{MN} \underline{w}_{\underline{n}}(f, \vartheta, \varphi) \cdot \underline{u}_{p,\underline{n},q} \\
&= \sum_{\underline{n}}^{MN} w_n(f, \vartheta, \varphi)\Theta_m^*(\vartheta, \varphi) \cdot u_{p,n,q}\Theta_m(\vartheta_p, \varphi_p) \\
&= \{\sum_{n=1}^{N} w_n(f, \vartheta, \varphi) \cdot u_{p,n,q}\} \\
&\quad \cdot \{\sum_{m=0}^{M-1} \Theta_m^*(\vartheta, \varphi)\Theta_m(\vartheta_p, \varphi_p)\} \\
&= v_{p,q}(f, \vartheta, \varphi) \cdot v_p^{iso}(f, \vartheta, \varphi),
\end{aligned} \tag{B.5}$$

where $v_{p,q}(f, \vartheta, \varphi)$ is the beampattern term of the subarray defined in (A.3) and $v_p^{iso}(f, \vartheta, \varphi)$ is the beampattern of the array composed of isotropic antennas for the p-th path, which is expressed as

$$\begin{aligned}
v_p^{iso}(f, \vartheta, \varphi) &= \sum_{m=0}^{M-1} \Theta_m^*(\vartheta, \varphi)\Theta_m(\vartheta_p, \varphi_p) \\
&= \sum_{m=0}^{M-1} \exp\{j[\mathbf{k}(f, \vartheta_p, \varphi_p) - \mathbf{k}(f, \vartheta, \varphi)] \cdot \underline{\mathbf{r}}_m\}.
\end{aligned} \tag{B.6}$$

Appendix C

The $v_p^{iso}(f, \vartheta, \varphi)$ for uniform arrays can be formulated as

$$v_p^{iso}(f, \vartheta, \varphi) = S_x \cdot S_y \cdot S_z, \tag{C.1}$$

where S_x, S_y and S_z are the beampatterns of ULA along x-axis, y-axis and z-axis, respectively, which can be further simplified as

$$\begin{aligned}
S_\Lambda &= \sum_{m_\Lambda=1}^{M_\Lambda} \exp[j(m_\Lambda - 1) * \Psi_\Lambda] \\
&= \frac{1}{M_\Lambda} \frac{\sin(\frac{M_\Lambda}{2}\Psi_\Lambda)}{\sin(\frac{\Psi_\Lambda}{2})} \\
\Lambda &\in \{x, y, z\},
\end{aligned} \tag{C.2}$$

where

$$\begin{aligned}
\Psi_x &= \frac{2\pi f \underline{d}_x}{c}(\cos\vartheta_p \cos\varphi_p - \cos\vartheta \cos\varphi) \\
\Psi_y &= \frac{2\pi f \underline{d}_y}{c}(\cos\vartheta_p \sin\varphi_p - \cos\vartheta \sin\varphi) \\
\Psi_z &= \frac{2\pi f \underline{d}_z}{c}(\sin\vartheta_p - \sin\vartheta) \\
M &= M_x \times M_y \times M_z
\end{aligned} \tag{C.3}$$

In the above equation, $\underline{d}_\Lambda$ and M_Λ are the distances between two adjacent subarrays and subarray numbers along Λ-axis, respectively, where $\Lambda \in \{x, y, z\}$.

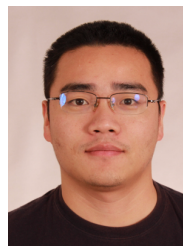## References

[1] T. S. Rappaport, S. Sun, R. Mayzus, H. Zhao, Y. Azar, K. Wang, G. N. Wong, J. K. Schulz, M. Samimi, and F. Gutierrez, "Millimeter wave mobile communications for 5g cellular: It will work!" *IEEE access*, vol. 1, pp. 335–349, 2013.

[2] M. Agiwal, A. Roy, and N. Saxena, "Next generation 5G wireless networks: A comprehensive survey," *IEEE Communications Surveys and Tutorials*, vol. 18, no. 3, pp. 1617–1655, 2016.

[3] E. G. Larsson, O. Edfors, F. Tufvesson, and T. L. Marzetta, "Massive mimo for next generation wireless systems," *IEEE Communications Magazine*, vol. 52, no. 2, pp. 186–195, 2014.

[4] T. E. Bogale and L. B. Le, "Massive MIMO and mmWave for 5G Wireless HetNet: Potential Benefits and Challenges," *IEEE Vehicular Technology Magazine*, vol. 11, no. 1, pp. 64–75, 2016.

[5] J. Zhang, G. Liu, F. Zhang, L. Tian, N. Sheng, and P. Zhang, "Advanced International Communications," *IEEE Vehicular Technology Magazine*, vol. 6, no. 2, pp. 92–100, 2011.

[6] J. Zhang, C. Pan, F. Pei, G. Liu, and X. Cheng, "Three-dimensional fading channel models: A survey of elevation angle research," *IEEE Communications Magazine*, vol. 52, no. 6, pp. 218–226, 2014.

[7] S. Payami and F. Tufvesson, "Channel measurements and analysis for very large array systems at 2.6 GHz," *2012 6th European Conference on Antennas and Propagation ({EUCAP})*, pp. 433–437, 2012.

[8] H. Yu, Q. Zheng, Z. Zheng, L. Tian, and Y. Wu, "The Rationality Analysis of Massive MIMO Virtual Measurement at 3.5 GHz," *Communications in China (ICCC Workshops), 2016 IEEE/CIC International Conference on*, 2016.

[9] J. Hoydis, C. Hoek, T. Wild, and S. ten Brink, "Channel measurements for large antenna arrays," *Wireless Communication Systems (ISWCS), 2012 International Symposium on*, pp. 811–815, 2012.

[10] X. Gao, O. Edfors, F. Rusek, and F. Tufvesson, "Massive mimo performance evaluation based on measured propagation data," *IEEE Transactions on Wireless Communications*, vol. 14, no. 7.

[11] À. O. Martínez, E. De Carvalho, J. Ø. Nielsen, and L. Jing, "Frequency dependence of measured massive mimo channel properties," in *Vehicular Technology Conference (vtc Spring), 2016 IEEEMa*, 2016.

[12] H. Xu, V. Kukshya, and T. S. Rappaport, "Spatial and temporal characteristics of 60-GHZ indoor channels," *IEEE Journal on Selected Areas in Communications*, vol. 20, no. 3, pp. 620–630, 2002.

[13] M. Samimi, K. Wang, Y. Azar, G. N. Wong, R. Mayzus, H. Zhao, J. K. Schulz, S. Sun, F. Gutierrez, and T. S. Rappaport, "28 ghz angle of arrival and angle of departure analysis for outdoor cellular communications using steerable beam antennas in new york city," in *Vehicular Technology Conference (VTC Spring), 2013 IEEE 77th*. IEEE, 2013, pp. 1–6.

[14] W. Li, L. Liu, C. Tao, Y. Lu, J. Xiao, and P. Liu, "Channel measurements and angle estimation for massive mimo systems in a stadium," in *2015 17th International Conference on Advanced Communication Technology (ICACT)*. IEEE, 2015, pp. 105–108.

[15] J. Fühl, J. P. Rossi, and E. Bonek, "High-resolution 3-D direction-of-arrival determination for urban mobile radio," *IEEE Transactions on Antennas and Propagation*, vol. 45, no. 4, pp. 672–682, 1997.

[16] J. Medbo, H. Asplund, J. E. Berg, and N. Jalden, "Directional channel characteristics in elevation and azimuth at an urban macrocell base station," *Proceedings of 6th European Conference on Antennas and Propagation, EuCAP 2012*, pp. 428–432, 2012.

[17] J. Medbo, H. Asplund, and J. E. Berg, "60 ghz channel directional characterization using extreme size virtual antenna array," in *Personal, Indoor, and Mobile Radio Communications (PIMRC), 2015 IEEE 26th Annual International Symposium on*. IEEE, 2015, pp. 176–180.

[18] W. Fan, I. Carton, J. Ø. Nielsen, K. Olesen, and G. F. Pedersen, "Measured wideband characteristics of indoor channels at centimetric and millimetric bands," *EURASIP Journal on Wireless Communications and Networking*, no. 1, p. 58, 2016.

[19] C. Gentile, S. M. López, and A. Kik, " A Comprehensive Spatial-Temporal Channel Propagation Model for the Ultrawideband Spectrum 2-8 GHz ," *IEEE Transactions on Antennas and Propagation*, vol. 58, no. 6, pp. 2069–2077, 2010.

[20] C. Wang, J. Zhang, L. Tian, M. Liu, and Y. Wu, "The variation of clusters with increasing number of antennas by virtual measurement," in *EuCAP*, 2017.

[21] C. Wang, J. Zhang, H. Yu, L. Tian, M. Liu, X. Ma, and Y. Wu, "The spatial evolution of clusters in massive mimo mobile measurement at 3.5 ghz," in *Vehicular Technology Conference*, 2017.

[22] K. Kalliola, H. Laitinen, L. I. Vaskelainen, and P. Vainikainen, "Real-time 3-D spatial-temporal dual-polarized measurement of wideband radio channel at mobile station," *IEEE Transactions on Instrumentation and Measurement*, vol. 49, no. 2, pp. 439–448, 2000.

[23] C. A. Balanis, *Antenna theory: analysis and design*. John Wiley & Sons, 2016.

[24] K. Woelder and J. Granholm, "Cross-polarization and sidelobe suppression in dual linear polarization antenna arrays," *IEEE transactions on antennas and propagation*, vol. 45, no. 12, pp. 1727–1740, 1997.

[25] R. J. Mailloux, *Phased array antenna handbook*. Artech House Boston, 2005, vol. 2.

Wei Fan received his Bachelor of Engineering degree from Harbin Institute of technology, China in 2009, Master's double degree with highest honours from Politecnico di Torino, Italy and Grenoble Institute of Technology, France in 2011, and Ph.D. degree from Aalborg University, Denmark in 2014. From February 2011 to August 2011, he was with Intel Mobile Communications, Denmark as a research intern. He conducted a three-month internship at Anite telecoms oy, Finland in 2014. His main areas of research are over the air testing of multiple antenna systems, radio channel sounding, modeling and emulation.

Jianhua Zhang , IEEE senior member. Now she is the Drafting Group (DG) Chairwoman of ITU-R IMT-2020 channel model. She received her Ph.D. degree in circuit and system from Beijing University of Posts and Telecommunication (BUPT) in 2003 and now is professor of BUPT. She has published more than 100 articles in referred journals and conferences and 40 patents. She was awarded 2008 Best Paper of Journal of Communication and Network. In 2007 and 2013, she received two national novelty awards for her contribution to the research and development of Beyond 3G TDD demo system with 100Mbps@ 20MHz and 1Gbps@100MHz respectively. In 2009, she received the "second prize for science novelty" from Chinese Communication Standards Association for her contribution to ITU-R 4G (ITU-R M.2135) and 3GPP Relay channel model (3GPP 36.814). From 2012 to 2014, she did the 3 dimensional (3D) channel modeling work and contributed to 3GPP 36.873 and is also the member of 3GPP "5G channel model for bands up to 100 GHz". Her current research interests include 5G, artificial intelligence, data mining, especially in massive MIMO and millimeter wave channel modeling, channel emulator, OTA test and etc.

Gert Frølund Pedersen was born in 1965 and married to Henriette and have 7 children. He received the B.Sc. E. E. degree, with honour, in electrical engineering from College of Technology in Dublin, Ireland in 1991, and the M.Sc. E. E. degree and Ph. D. from Aalborg University in 1993 and 2003. He has been with Aalborg University since 1993 where he is a full Professor heading the Antenna, Propagation and Networking LAB with 36 researcher. Further he is also the head of the doctoral school on wireless communication with some 100 phd students enrolled. His research has focused on radio communication for mobile terminals especially small Antennas, Diversity systems, Propagation and Biological effects and he has published more than 175 peer reviewed papers and holds 28 patents. He has also worked as consultant for developments of more than 100 antennas for mobile terminals including the first internal antenna for mobile phones in 1994 with lowest SAR, first internal triple-band antenna in 1998 with low SAR and high TRP and TIS, and lately various multi antenna systems rated as the most efficient on the market. He has worked most of the time with joint university and industry projects and have received more than 12 M$ in direct research funding. Latest he is the project leader of the SAFE project with a total budget of 8 M$ investigating tunable front end including tunable antennas for the future multiband mobile phones. He has been one of the pioneers in establishing Over-The-Air (OTA) measurement systems. The measurement technique is now well established for mobile terminals with single antennas and he was chairing the various COST groups (swg2.2 of COST 259, 273, 2100 and now ICT1004) with liaison to 3GPP for over-the-air test of MIMO terminals. Presently he is deeply involved in MIMO OTA measurement.

Fengchun Zhang received her B.Sc. degree in optical information science and technology, and the M. Sc. in acoustics from the South China University of Technology, Guangzhou, China, in 2006 and 2009, respectively. She is currently a Ph.D. fellow with the Department of Electronics Systems, Aalborg University, Aalborg, Denmark. Her research interests are in antenna array signal processing, beamforming, parameter estimation for channel characterization of centimeter and millimeter wave wireless systems.